Side Force Computations for Slender Bodies by a Far-Field Approach

Y. Y. Chan*
National Research Council, Ottawa, Canada

Calculations of the side forces and moments acting on a slender body at high angles of attack are presented. The procedure is based on a model that relates the far-field wake structure in the form of a system of vortex filaments to the induced forces. The geometry of the vortices as required by the inner boundary conditions is derived from experimental data with laminar separation. The circulation of the vortices is determined by the dynamics of the vortex system. Enhancement of the vortex strength by the nose shape is also considered. The model has been successfully applied to bodies with ogive noses. The concept is general and can be applied in principle to different separation conditions and nose shapes, provided the inner conditions for these cases are properly specified.

Nomenclature

A = area
C_n = yawing moment coefficient
C_N = normal force coefficient
C_p = pressure coefficient
C_Y = side force coefficient
D = diameter of the cylindrical body
g = vortex location
h = lateral separation of vortex rows
h_p = lateral distance of vortex row to the body centerline
K = vortex strength
ℓ_n = nose length
ℓ_v = length of first vortex segment
L = total body length
q = induced velocity
r = radial axis for cylindrical polar coordinate
s = distance from the vortex liftoff point to a point downstream
S = vortex Strouhal number in impulse flow analogy
t = time parameter in impulse flow analogy
U = freestream velocity
x,y,z = rectangular coordinates
α = angle of attack
δ = vortex inclination, first segment
ϵ = slenderness ratio
σ = vortex inclination, second segment
χ = ratio of tangents of vortex inclination to angle of attack
ϕ = perturbation velocity potential

I. Introduction

THE side force acting on a long slender body at high angles of attack has been known to be induced by the asymmetric vortex shedding on the lee side of the body. The vortices are formed from the rolling up of the free shear layers originating from the three-dimensional separations of the boundary layer along the body. The development of the three-dimensional boundary layer over the body is extremely sensitive to the body geometry and surface conditions, transition, and the external inviscid flowfield that consists of the cascade of the shedded vortices. A complete analysis of such a complicated flow dominated by the viscous-inviscid interaction is certainly a major task, and the prediction methods presented up to date are therefore based on the full- or semi-empirical approaches. Reviews of the subject have been given by Wardlaw,[1] Hunt,[2] and Ericsson and Reding.[3,4] The physical nature of the flow is well described by Hunt and Ericsson and Reding, and a thorough account of the prediction methods can be found in the work by Wardlaw.

The three-dimensional viscous flow that leads to the vortex shedding is indeed complex. However, once the shear layers separate from the body, they roll up into a simple and clearly spaced system of concentrated vortices. The vortex system is essentially inviscid and can be modeled with discrete potential vortices for the analysis of the flow. If the body is sufficiently long, the flow pattern varies slowly along the body, and the local flow can be treated as two-dimensional in the crossflow plane. Most of the prediction methods are based on this approach.

Away from the body, the vortex system can be considered as a number of trailing vortex filaments, the arrangement of which depends on the dynamics of the vortices and the conditions of the vortex shedding at the body. The interdependence of the near and far fields can be explicitly delineated by an asymptotic analysis of the flow regions. The analysis is given in the Appendix, in which the asymptotic equations and the boundary conditions are derived. The analysis provides a justification of the crossflow method of solution for the near field and the definition of the far-field boundary value problem. The far-field formation is adopted later for the analysis of the relation between the side force and the wake structure.

Of all the prediction methods, the method by Lamont and Hunt is the only one that can predict the maximum force envelope in realistic agreement with the experimental measurements.[1,5] The method is based on the correlations of the experimental data obtained by the authors in a series of experiments at low Reynolds numbers with laminar separations. The crux of the success of the method is the establishment of the side force distribution along the body with respect to the angles of attack and nose configurations. The physical relations behind these empirical expressions, however, have not been addressed in the paper. Therefore, it is difficult to extend the method to cover different flow conditions or body configurations.

To advance and broaden the scope of the empirical prediction method, it is necessary to understand the physics behind the empirical conditions, i.e., the relations between the force distribution and the structure of the wake. This paper at-

Received Sept. 26, 1986; revision received April 9, 1987.

*Senior Research Officer, High Speed Aerodynamics Laboratory. Member AIAA.

tempts to establish such a relation. The technique used simulates the wake structure with a numerical model. A simple model is first set up for the far-field structure of the wake in a form of a system of trailing vortices. The arrangement of the vortex filaments at the inner boundary is provided by data from a number of experiments. The circulations of the vortices are determined by the dynamics of the vortex system. The induced flowfield, hence the sidewash to the body due to the vortices, can then be evaluated. The side force is determined from the tilted force vector with the normal force assumed to be known. The side forces thus obtained are shown to be in agreement with the experimental data. The proposed model can be considered to closely reproduce the essential physical characteristics of the flow, and the sought relation is thus established. The relation so derived is general in nature, and the dependency on specific conditions appears only in the inner boundary conditions. It can therefore be applied to cases with conditions and configurations different from those used in the numerical experiment, provided the inner boundary conditions are known.

The procedure proposed herein constitutes a prediction method that has a wider scope than those based entirely on empirical correlations. Configurations with ogive noses are considered in some detail in this paper. Applications to a body with a conical nose are in progress, and the results will be presented in a separate paper.

II. Formulation

Experimental observations have shown that for a long slender body at high angles of attack, the vortices from the separated shear layers roll up, leaving the body at a small angle inclined to the body axis and then turning rapidly toward the freestream direction downstream. Away from the body, the vortices can be considered as concentrated vortex filaments that in turn induce a flowfield around the body. If the vortex pattern is asymmetric, the induced flowfield at the body, now shrunk to a line, will tilt the incidence velocity vector away from its original direction, resulting in a force component in the lateral direction. This observation is supported by experimental results, which show that the inclination of the resultant force from the incidence plane (y-z plane) is closely proportional to the magnitude of the side force.[6] Thus, if the normal force is known, either from experimental data or from prediction by a computational method,[7] what remains is to determine the sidewash angle indicating the amount of rotation of the resultant force vector.

A simple vortex system is now assumed, as shown in Fig. 1. A row of vortices is situated at each side of the body. The vortices are shed alternately from one side and then the other and are rotating in opposite directions. The curved vortex filament is modeled by two straight segments for simplicity in analysis. The first segment makes an angle δ with the body axis and has a length ℓ_v and the second segment continues from the kink and extends to infinity, with an angle of inclination σ. The sidewash induced by the vortex filament at a point P located at the body axis can be derived from the expression for a straight line vortex.[8] For the leading segment, the induced velocity in the y direction is

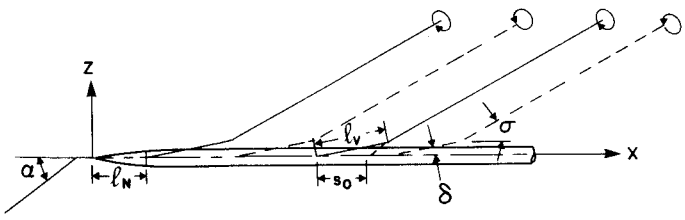

Fig. 1 Model of vortical wake from long slender body at high incidence.

$$q_Y = \frac{K}{4\pi D}\frac{s\sin\delta}{s^2\sin^2\delta + h_p^2} \times \left[\frac{s\cos\delta}{\sqrt{s^2+h_p^2}} + \frac{\ell_v - s\cos\delta}{\sqrt{\ell_v^2 - 2\ell_v s\cos\delta + s^2 + h_p^2}}\right] \tag{1}$$

where s is the distance along the body axis measured from the vortex liftoff point to P, h_p is the lateral distance from P to the plane of vortex row, and K is the circulation of the vortex considered. For the trailing part of the vortex, the expression is given as

$$q_Y = \frac{K}{4\pi D}\frac{s_m\sin\sigma}{s_m^2\sin^2\sigma + h_p^2} \times \left[1 + \frac{s_m\cos\delta - x_m}{\sqrt{(s_m\cos\delta - x_m)^2 + s_m^2\sin^2\sigma + h_p^2}}\right] \tag{2}$$

with

$$s_m = s - s_o$$

$$x_m = \frac{s_o\tan\delta}{(\tan\sigma - \tan\delta)\cos\sigma}$$

where s_o is the distance from the starting point of the vortex to the intersection point of the downward extension of the trailing vortex line with the x-y plane. All the length variables have been normalized by the maximum body diameter D.

With a staggered vortex system, as shown in Fig. 1, the sidewash induced along the body varies oscillatorily. If only the trailing vortex is used, without the leading portion, the wave form of the oscillatory sidewash approaches a square, and the zero crossings are close to the locations of the vortex liftoff points along the x axis. With the leading portion of the vortex, the resulting wave form is nearly sinusoidal and is closely similar to that observed in the experiments of Ref. 9. The zero crossings also move away from the vortex locations.

The side force is related to the normal force and the sidewash angle ϕ by

$$F_Y = F_N\tan\phi \tag{3}$$

Experimental measurements show that the local normal force does not vary appreciably along the cylindrical part of the body.[9] Thus, the side force can be directly locally related to the sidewash. The sidewash angle is then calculated from the mean sidewash velocity along the body and the crossflow velocity. The total side force can be written as

$$C_Y = \frac{C_N}{U\sin\alpha}\frac{1}{L}\int_o^L dq_Y dx \tag{4}$$

where C_N and C_Y are the coefficients of the normal and the side forces, respectively, d is the local body diameter, L the body length, α the angle of attack, and U the freestream velocity. The yawing moment can be similarly derived as

$$C_n = \frac{C_N}{U\sin\alpha}\frac{1}{L}\int_o^L dq_Y(x_m - x)dx \tag{5}$$

where x_m is the location of the reference center of the moment.

To determine the distribution of the sidewash along the body, it is necessary to know the number of vortices, the vortex geometries, and their circulations. The information for the first two items has to be drawn from experimental correlations. Once the geometries of the vortices are known,

the circulation can be determined by the dynamics of the vortex system.

III. Vortex Geometry

A large amount of experimental data on the characteristics of the vortex system have been compiled in Ref. 1. The correlations of the experimental data show that most of the parameters are configuration-dependent. It is necessary, therefore, to choose a particular configuration for the development of the present approach. The configuration consisting of a long cylindrical body and an ogive nose is found to be preferable in that the detailed experimental measurements and parametric correlations for such a configuration, as given in Refs. 5 and 9, allow a precise modeling of the vortex system.

To construct the vortex system, some parameters applied generally to different configurations are taken from the correlation curves of Ref. 1. Those depending on the nose shape are taken from Refs. 5 and 9. These parameters are discussed as follows.

A. Shedding Frequency

The vortex shedding frequency in terms of Strouhal number S is practically constant for a crossflow Mach number less than 0.7. The value of 0.2 is taken for the present use from Fig. 22 of Ref. 1.

B. Vortex Inclination

The ratio of the inclination of the trailing vortex and the incidence of the body χ are functions of the crossflow Mach number. For low subsonic flows, the value of χ is taken to be 0.8 from Fig. 23 of Ref. 1. The leading vortex inclination is not available from the experimental data. However, based on the flow visualizations of Clark,[10] it is assumed to be one-fifth of the trailing vortex angle for the present formulation. A small variation of this ratio does not appreciably affect the wave form of the sidewash distribution.

C. Vortex Locations

The locations of the vortices depend on the shedding frequency, the angle of attack, and the Mach number. These related variables can be grouped into a parameter $(g\text{S}\tan\alpha/D)$, which correlates well with the crossflow Mach number, as shown in Fig. 25 of Ref. 1. The symbol g is the vortex location, defined as the intersection of the main vortex line with the body axis measured from the nose of the body. The correlations, however, show a strong dependency on the nose shape, especially for the first two vortices. Since the vortex locations directly affect the sidewash distribution along the body, it is preferable that the data given in Refs. 5 and 9 be employed directly. It should be noted that the experiments in Ref. 9 were performed at low Reynolds numbers and that laminar separation occurred on the model. Thus, the conditions derived for present use are restricted to flow with laminar separations.

In the experiments of Lamont and Hunt, the side force distribution, but not the vortex positions, have been measured. Therefore, it is necessary to deduce the vortex positions from the side force distribution. This is achieved by assuming the positions of the vortices and then matching the sidewash wave form generated by the vortex model to the sinusoidal wave form of the side force distribution given in Fig. 1 of Ref. 5. The parameters chosen to be matched are the zero crossings and the ratios of the peaks of the three dominating half-cycles in the orders of $1.0:-0.6:0.3$. To match the decaying wave form, the strengths of the vortices have to be in decreasing order, and the resulting ratios for the first four vortices are 1.0, 0.8, 0.4, 0.4. The sidewash distribution and the vortex locations are shown in Fig. 2 for a typical case. The wave form generated is very similar to that given in Ref. 5, the zero crossings of which are also shown in the figure. Based on this procedure, the vortex system is constructed as follows: The first vortex starts at t_A (the first zero crossing of the side force wave form of Ref. 5) and turns upward (the second segment) at a point two-thirds of the first wavelength, t_{AC}. The second vortex starts at the location where the first vortex turns upward and extends to a distance equal to the second half-wavelength, t_{CE}, then turns upward. Thus, as the upstream vortex turns upward, a new vortex starts at the other side. The rest of the vortices downstream are formed in a similar manner and keep the same distance apart. These correlation parameters $(t = x\tan\alpha/D)$ are given as

$$t_A = 1.5 + 0.025\alpha \quad \text{to} \quad t_A = 3.5 - 0.5\ell_n$$

$$t_C = 5.5 + 2.35\tan\alpha \quad \text{to} \quad t_C = 10.5 - \ell_n$$

$$t_{CE} = 2 + 1.3\tan\alpha \tag{6}$$

where ℓ_n is the normalized nose length. This assumed correlation of the vortex position and the sidewash distribution is qualitatively substantiated by the recent experimental results of Champigny.[11] With these correlations, the locations of the vortices are now a function of the angle of attack and nose length. The correlation parameters of the wave form and the vortex locations along the body are plotted against the angle of attack in Fig. 3. For the present model, only the asymmetrical vortices are considered, and the pair of weak near-symmetrical vortices from the nose has been neglected.

D. Lateral Spacing of Vortices

The lateral spacing between the vortex rows on either side of the body is taken from Ref. 16 as

$$\frac{h}{D} = 0.19\,\frac{\chi}{S} \tag{7}$$

For the present case, h/D is taken to be 0.76.

E. Number of Vortices

As the angle of attack increases, the first asymmetrical vortex will form from the body and a side force is generated. The incipient angle of attack depends strongly on the configuration. A collection of data is given in Ref. 1 for a number of nose geometries and body lengths. For the present case, the formula given by Lamont and Hunt[5,9] is used. At higher angles of attack, the first asymmetric pair of vortices moves upstream, and more vortices are formed downstream

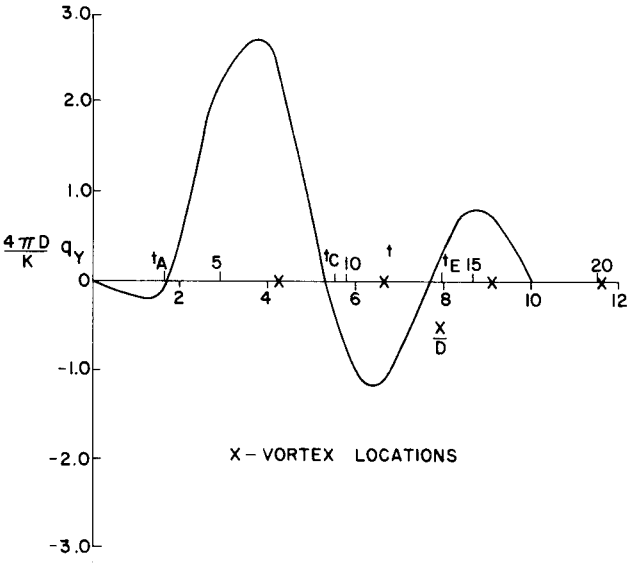

Fig. 2 Sidewash distribution and vortex locations along the body ($\alpha = 60$ deg); t_A, t_C, and t_E are defined in Eq. (5).

in sequence. For low-speed flows, only a small number of vortices has been observed.[10] This is consistent with the measured side force distributions, which show that only three half-cycles are significant.[9] Thus, for the present case, the number of vortices is limited to four.

Vortices are added to the system discretely in the present model. An additional vortex is introduced when the distance from the last existing vortex location to the base of the body is larger than half the spacing between that vortex and the next (fictitious) vortex downstream. The distance between the vortices can be obtained from the vortex spacing given in Fig. 3 for a given angle of attack.

IV. Dynamics of Vortices and Circulation

Once the geometry of the vortices is specified, the circulation of the vortices is determined by the dynamics of the vortex system. The analysis of the vortex system is carried out in the far field, taking advantage of the simple and orderly arrangement of the vortex filaments. Considering a vortex filament in the system, the geometric relation of the vortex orientation to the body in the flowfield yields[12]

$$\frac{q_v}{U\sin\alpha}=\frac{1-\chi}{\cos(\alpha-\sigma)} \tag{8}$$

where

$$\chi=\frac{\tan\sigma}{\tan\alpha}$$

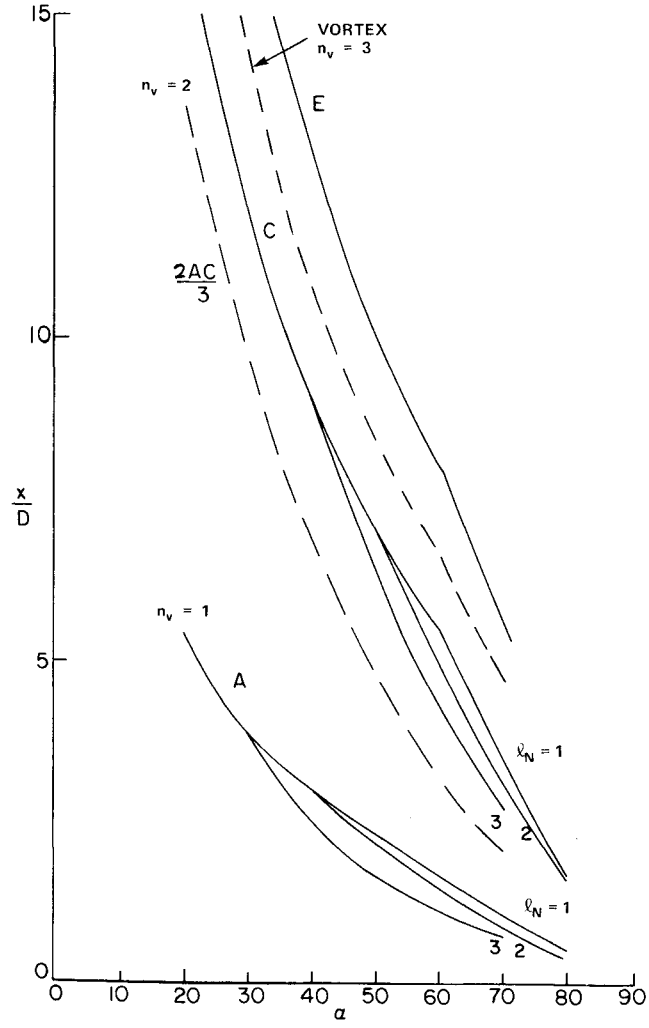

Fig. 3 Parameters defining vortex locations, t_A, t_B, and t_E, expressed explicitly along the body against angle of attack.

and q_v is the velocity of the vortex in the x-z plane induced by all other vortices.

The induced velocity can be written in a manner similar to that of Eq. (1), but at a direction normal to the vortex in the x-z plane. In the far field, for the pth vortex,

$$q_v^{(p)}=\sum_{n=1}^{N}\frac{K_n}{2\pi D}\frac{h}{(x_p-x_n)^2\sin^2\sigma+h^2} \tag{9}$$

where x_p and x_n are the locations of the pth and nth vortices along the x axis, respectively. With the geometric relation Eq. (8), the circulation can be written as

$$\frac{K}{2\pi DU\sin\alpha}=\frac{1-\chi}{\cos(\alpha-\sigma)}\frac{1}{h}\left[\sum_{n=1}^{N}\frac{k_n}{(x_p-x_n)^2\sin^2\sigma+h^2}\right]^{-1} \tag{10}$$

where k_n is the ratio of the nth vortex strength with respect to the maximal value K. The circulation of the second vortex as determined by the preceding expression is taken to be the vortex strength of the system. Equation (10) indicates that the vortex strength decreases as the number of vortices increases. If the vortex row extends to infinity both upstream and downstream, Eq. (10) is reduced to the form for a Karman's vortex street given by Thomson and Morrison.[12] It can be shown that the vortex strength approaches that of the vortex street with only three vortices in the system. Further addition of vortices changes the circulation only slightly.

For each vortex filament, the vorticity decays along the vortex itself as it trails downstream. In the derivation of the sidewash velocity, Eq. (1), the vortex strength is assumed to be constant along the vortex. Because of the vortex decay, a reduction fraction of 0.5 is used to modify the vortex strength, which is equivalent to assuming a linear decay to zero at infinity.

V. Further Modulation of the Vortex Strength

The discussion of the vortex strength in the preceding section is based on the nature of the vortex system and is generally applicable to any long, slender, cylindrical body. The side force development, however, is known to be strongly affected by the shape of the nose and the vortex movement. These additional factors modulating the vortex strength are discussed as follows.

A. Effects of Nose Shape

The vortices originate from the separations of the three-dimensional boundary layer that develops from the nose of the body. The shape of the nose directly controls not only the vortex position, as already shown in Fig. 3, but the vortex strength as well. Thus, the side force development is drastically influenced by the nose shape, as illustrated by Lamont and Hunt.[5] The nose effect on the vortex strength can be estimated qualitatively from the relation of the circulation of the vortex to the vorticity of the shear layer at the nose region from which the vortex originates.

It has been discussed by Lamont and Hunt[9] that additional vorticity is generated due to the expansion of the flow over the nose region. This increased vorticity will be fed into the vortices downstream, altering their strengths. The expanding flow over the nose is also responsible for the normal force generated there. Thus, it is assumed that the increase of vorticity is related to the normal force at the nose region. This relation is employed herein for the estimation of the nose effect on the vortex strength.

The normal force acting on the portion of the nose section from the start of the vortex to the cylinder junction can be evaluated by the crossflow method as[7]

$$C_{N_n}=\sin 2\alpha\cos\frac{\alpha}{2}\left[1-\frac{A_1}{A_j}\right]+C_{D_n}\sin^2\alpha\frac{Ap_{1j}}{A_j} \tag{11}$$

where subscript 1 denotes a nose section normal to the body axis and j at the nose/body junction. The cross-sectional area of the nose at the location indicated by the subscripts is A. The projected area between stations 1 and j in the x-y plane is A_p. In real flows, the influence of the nose extends beyond the nose into the front portion of the afterbody. This extension of the nose influence depends on the severity of the pressure gradient over the nose, which is strong for a short nose and weak for a long one. The effect is taken into account by multiplying the nose normal force factor C_{N_n} with an empirical coefficient C_{FN}. The factor that accounts for the increase of vorticity due to the nose shape is thus

$$F_n = 1 + C_{FN} C_{N_n} \tag{12}$$

where the coefficient C_{FN} is assumed to be a linear function of the nose length as

$$C_{FN} = 3 - 0.5\ell_n \tag{13}$$

for the present cases. The empirical factors are chosen to give a proper match of the nose effects to those given in Fig. 4 of Ref. 5.

B. Vortex Transition Effect

At very high angles of attack, the side force decays rapidly. The decay is due to the transition of the flow pattern from that developing over the nose and the aft-body to that developing over an infinite cylinder. The averaged side force on the latter is zero.[9] Experimental evidence shows that the side force decreases to zero as the second vortex reaches the nose-cylinder junction. This empirical criterion is used to define a transition factor for the decay of the side force as

$$F_T = \frac{x_2 - x_j}{x_2 - x_1} \qquad x_1 < x_j \tag{14a}$$

$$= 1 \qquad x_1 \geq x_j \tag{14b}$$

where x_1, x_2, and x_j are the positions of the first and the second vortices and the nose junction, respectively. This simple relation will give a nonlinear decay factor with respect to the angle of attack as observed in Ref. 5. A more complicated expression is not warranted in view of the empirical nature of the approach and the limited data available.

C. Finite Length of the Body

For the present model, when the second vortex is initiated, only half of the leading vortex segment will be situated ahead of the base of the body (see Sec. III.E). The amount of vorticity feeding into the vortex is proportional to the length along which the vorticity is generated (Sec. V.A). Thus, a factor is introduced to account for the feeding length of the vortex. This factor is defined as

$$F_{\text{base}} = \frac{\ell_e - x_1}{x_2 - x_1} \qquad x_2 \geq \ell_e \tag{15a}$$

$$= 1 \qquad x_2 < \ell_e \tag{15b}$$

where ℓ_e is the effective length of the body. The flow downstream of the body base is allowed to expand, and this disturbance propagates upstream and affects the local flow on the body. This has the effect of making the body appear shorter, and an apparent body length is obtained by modifying the physical length by a factor of 0.8.

VI. Bodies with Ogive Noses

The preceding sections describe the details of the model for investigation of the relation of the vortical wake and the side force. The procedure starts at the angle of attack at which the vortex arrangement first becomes asymmetric and the side force sets in. For the cases considered with ogive noses, the starting incidence suggested by Lamont and Hunt[5] and given in Ref. 1 is used. Two vortices are assumed to exist at the starting incidence. The vortex positions as the angle of attack increases are given in Sec. III.C. The vortex strength as determined from Eq. (10) is then calculated. The final vortex strength is calculated by including the factors of the nose shape, Eq. (12), the vortex transition, Eq. (14), and the finite body length, Eq. (15). With the vortex strength known, the sidewash distribution is calculated from Eqs. (1) and (2). By integration, the total side force and the yawing moment are obtained by Eqs. (3) and (4), while the normal force is evaluated from the crossflow method[7] or from experimental data.

To verify the present model, all cases considered in Ref. 5 are computed herein. They are chosen because the method presented in the reference, though fully empirical, is the only method that can predict accurately the force and moment variations through the complete incidence range, including the effect of the nose length. These cases are now discussed as follows.

A. Case 1: $L = 12$; $\ell_n = 1,2,3$; $x_m = 6$

This case was used by Lamont and Hunt to demonstrate their prediction method, which accounted for the nose effects.[5] These examples are thus suitable for testing the present model and checking the basic assumptions of the formulation. The computed side forces and yawing moments for these examples are shown in Fig. 4. The results produce all features of the side force variation with incidence, and the explicit effects of the nose length are similar to those given in Ref. 5.

The variations of the side force and the moment with incidence can be readily examined in light of the present modeling of the vortical flow. The case with the shortest nose length is first considered. At the onset of the side force, two asymmetric vortices are formed, with the first vortex situated at the cylindrical body and the second trailing downstream. The flowfield is induced mainly by the first vortex, and the induced sidewash, the first loop of the wave form (see Fig. 2), is distributed over the cylindrical portion of the body. With the moment reference point at the middle of the body length, a negative moment results. As the incidence increases, the vortices move upstream and the vortex strength increases steadily, hence the increase of both the side force and the moment. At about 25-deg incidence, a third vortex is formed. With further increase of the incidence, the negative loop of the wave form appears near the end of the body, causing a slight drop of the force and a rapid reduction of the negative moment. The moment becomes positive as half of the first loop moves over the moment reference point. At about 45-deg incidence, a fourth vortex joins in, and the second positive loop of the wave form starts to load the body, causing a slight drop of the moment. At even higher incidences, the vortices move further upstream and the extent of the side loading along the body reduces, yielding a steady decrease of the force and moment. At about 70-deg incidence, the first vortex moves across the nose/body junction (see Fig. 3). The nose effect is felt, and the increase of the vortex strength is reflected by the slight growth of the force and the moment. As the first vortex moves upstream of the nose/body junction, the transitional process rapidly reduces the force and moment to zero. Since the nose effect is felt only at the very end, this case can be considered as that of vortical flow over a long cylindrical body. The results validate the basic concept of the present model.

For the cases with longer nose sections, $\ell_n = 2$ and 3, the vortex movement are only slightly different from the case of the short nose section, as shown in Fig. 3. However, the nose

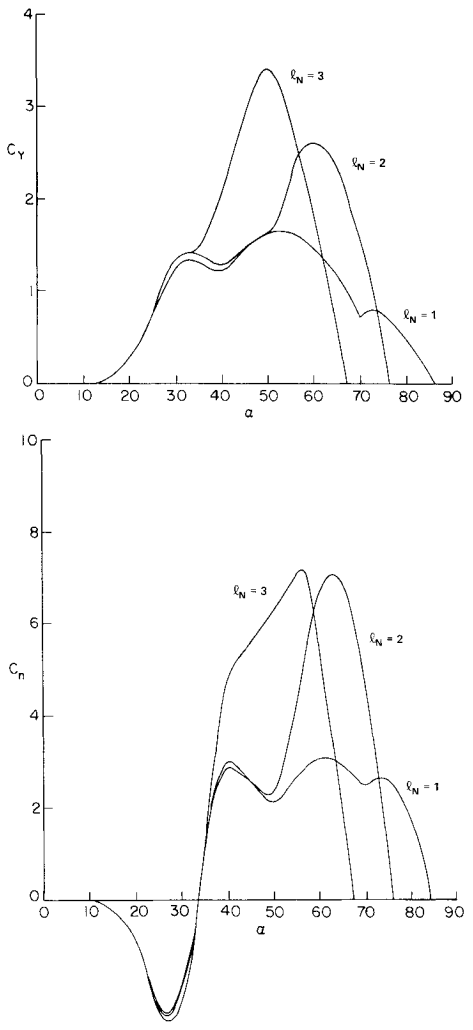

Fig. 4 Computed side force and yawing moment for a body with an ogive nose showing effect of nose fineness ratio.

effect is much stronger and is felt much sooner as the first vortex moves across the nose/body junction, which is now located further downstream from the apex of the nose. For the $\ell_n = 2$ case, the side force and the moment variations up to moderate angles of attack are nearly identical to those of the short-nose case. This is also indicated by the same vortex strengths, as the nose effect is not yet felt. At about 50-deg incidence, the nose effect sets in and the vortex strength increases rapidly. The transition effect also appears at the same incidence but does not severely reduce the vortex strength until 65 deg. After that, the vortex strength drops rapidly to zero at about 75 deg. For the case with $\ell_n = 3$, the nose effect sets in at about 35 deg and is much stronger than for the other cases, as shown both in the side force and the yawing moment. The experiments for this case were performed in low Reynolds number flows ($Re_D = 1.1 \times 10^5 \sin\alpha$) with laminar separations, and the normal force was not measured. Thus, the normal force required for the calculation of the side force in the present formulation was obtained by the crossflow method of Jorgensen.[7] The crossflow drag coefficient in the method, however, was replaced by that deduced from the correlation of experimental data of Case 2 for laminar separations.

The example with the nose length equal to 2 is replotted in Fig. 5 with the experimental data taken from Ref. 5. Only the upper and lower limits of the data points are shown in the graph. Both the predicted force and moment envelop the data well. The predictions of Ref. 5 are also plotted for comparison. The present results follow fairly closely those predicted in Ref. 5.

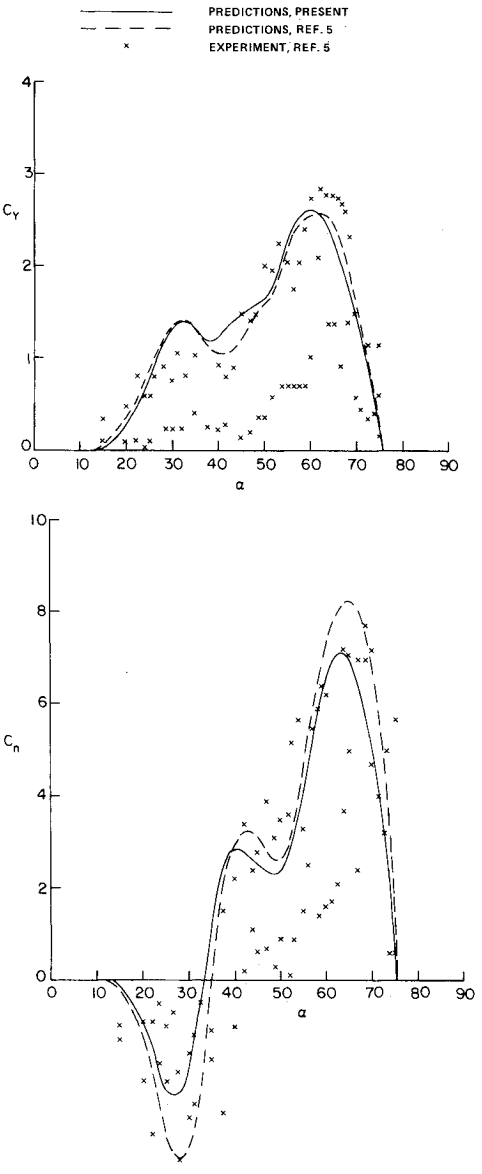

Fig. 5 Comparison of predicted side forces and yawing moments with experimental data of Ref. 5 for a body with an ogive nose; only the upper and the lower limits of the data are shown ($\ell_n = 2, L = 12$, $x_m = 6$).

The side force distributions along the body are shown in Figs. 6a-c. The curves from the method of Lamont and Hunt[5] correspond to the maximal possible values assumed in the method. The experimental data taken from Ref. 9, however, may not be at the maximal value, as the magnitude depends on the roll angle of the body. The shape of the distribution is not affected by the roll angle and can thus be used as a reference for checking the present model. The comparison shows that the present results are slightly out of phase from the data, indicating that the assumed vortex positions need some adjustment. The magnitude of the present result is lower than that of Ref. 5 but appears to agree better with experiment.

B. Case 2: $L = 15$; $\ell_n = 3$; $x_m = 8.179$

This case is taken from the experiment of Smith and Nunn[13] and is different from the previous case only by a greater body length. The experiment was again performed in low Reynolds number flows ($Re_D = 0.5 - 1.4 \times 10^5$) with laminar separation. The normal forces were measured and found to be Reynolds number dependent. The experimental data for the normal forces were used for the present com-

putation of the side forces. The results of the side force and yawing moment are presented in Fig. 7. The Reynolds number dependency of the side force comes directly from the normal force data. In the present form of the method, no provision has been made for empirical input due to Reynolds number variations. The predictions envelop the experimental data well, except at very high incidence, where the predicted values decay faster than the experimental data.

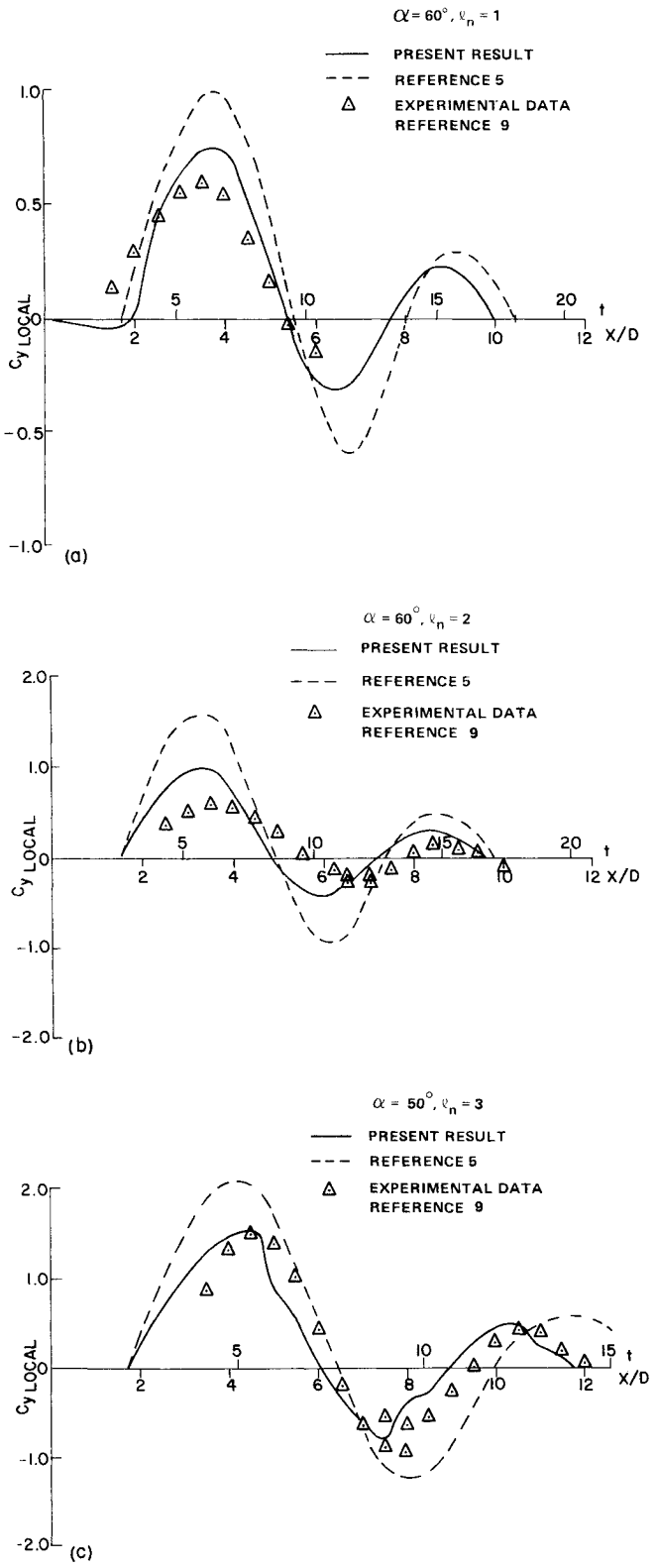

Fig. 6 Comparison of predicted side force distributions along a body with an ogive nose with experimental data of Ref. 9 for three nose lengths.

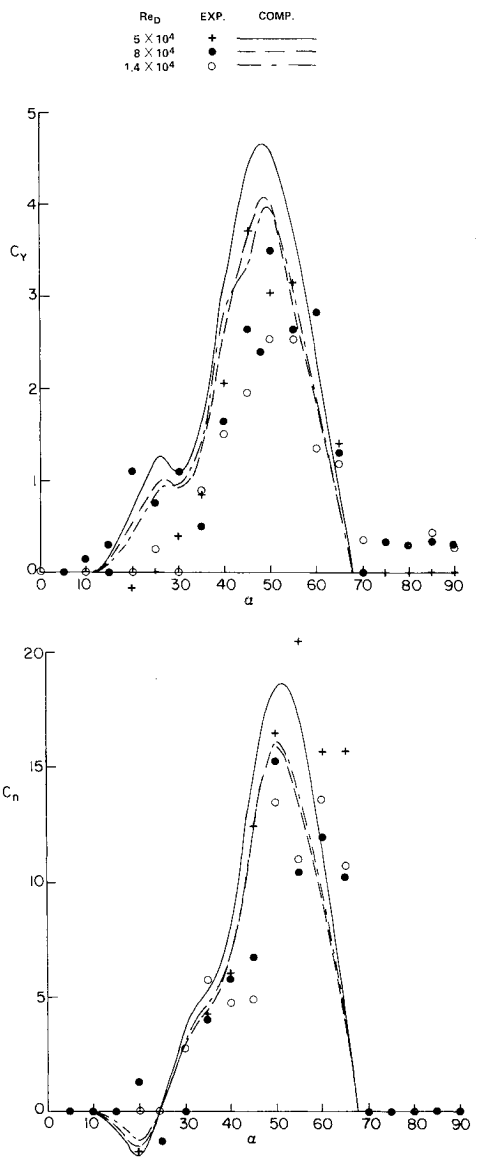

Fig. 7 Comparison of predicted side forces and yawing moments with experimental data of Ref. 13 for a body with an ogive nose ($\ell_n = 3$, $L = 15$, $x_m = 8.179$).

C. Case 3: $L = 7.0, 3.5$; $\ell_n = 3.5$; $x_m = 4.38$

The experiments of Coe, Chambers, and Letko[6] are of particular interest because data for the nose section alone and the angle of inclination of the resultant force are available. The first configuration considered had a nose and an aft-body and was basically the same as the cases just discussed, except for a shorter body length. The normal force data were not available for this case, and the force has been calculated from the crossflow method[7] with the crossflow drag coefficient adjusted for the experimental Reynolds number of 2.1×10^5. The predicted results are shown in Fig. 8. At moderate incidence, the side force increases steadily up to a 40-deg angle of attack and then drops off sharply, while the experimental results peak at about 50 deg. The computation shows that at 45-deg incidence, a third vortex is added to the system, reducing the side force and moment. The difference between the calculated results for the three-vortex system and experiments indicates that in the real flow, there may only be two vortices in the flowfield. The tuft grid surveys of the flowfield shown in Ref. 6 for this case show only two vortices within the limited area covered by the grid. By assuming only two vortices existing in the flowfield, the computed

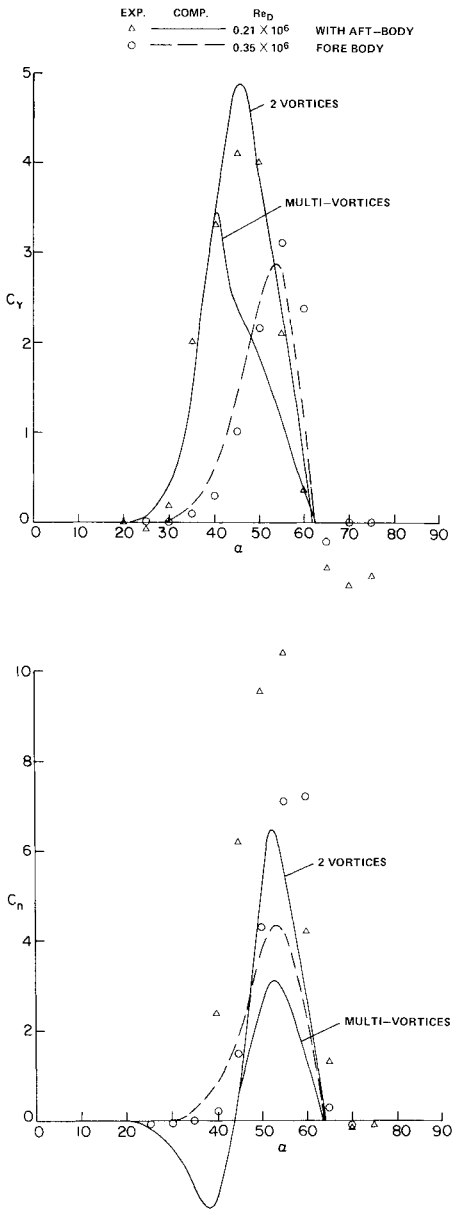

Fig. 8 Comparison of predicted side forces and yawing moments with experimental data of Ref. 6 for a body with an ogive nose and an ogive nose section alone ($\ell_n = 3.5$, $L = 3.5$; 7, $x_m = 4.38$).

results show much better agreement with the experimental data. The yawing moment, however, is underpredicted, and the experimental data do not show strong negative moments at moderate incidence.

The second configuration consists of the nose section alone. The normal force was measured in the experiment, and the data were used in the side force calculation. The present model generates only two vortices for the entire range of incidence in agreement with the experimental observation. In the computation, the base factor is set to unity, since there is no aft-body contribution to the vortex strength. The results are also shown in Fig. 8. The computed side force agrees reasonably well with the data, while the moment is again underpredicted. Figure 9 shows a comparison of the experimental and computational results of the inclinations of the resultant force. At moderate incidence, the angles are overpredicted, while at high incidence, they are underpredicted. However, the general trend of the computed results follows the experimental data reasonably well.

The three examples given demonstrate that the present model simulates the vortical flow fairly accurately and generates all the essential features of the force and moment variations. This model, therefore, establishes a relation between the side force distribution and the far-field structure of the wake and provides physical explanations for the variations of the former with respect to parameters such as incidence and nose configurations.

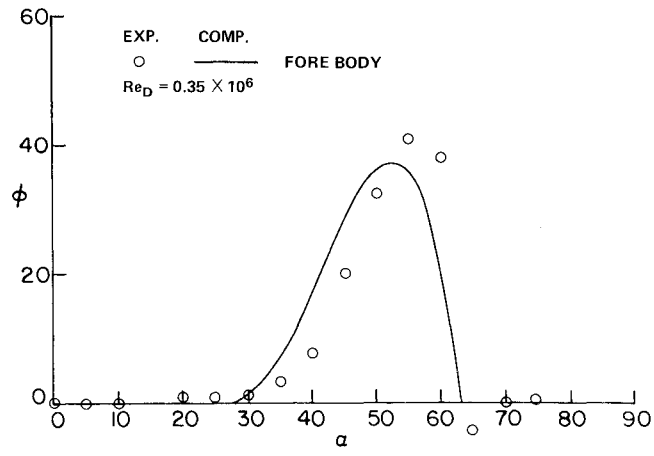

Fig. 9 Comparison of predicted inclination of resultant force for an ogive nose with experimental data of Ref. 6 ($\ell_n = 3.5$, $L = 3.5$).

VIII. Concluding Remarks

The establishment of a relation between the far-field wake and the side forces and moments has been demonstrated by the examples given in the last section. The basic formulation and the assumed conditions of the model can be further examined so that a general relation may emerge that leads to wider applications. The model is based on the far-field wake structure in the form of a system of vortex filaments. The geometry of the vortices is provided by a set of data taken from experiments with laminar separation. The circulation of the vortices is determined by the dynamics of the vortex system. The vortex strengths are enhanced by the additional vorticity from the nose, which is assumed to be related to the local normal force. With the consideration of the vortex decay, the simple model is completed. The formulation is general in nature, except that the inner boundary conditions have been derived from specific experimental results. The present results can therefore be interpreted to show that if the vortex geometry is known, the induced flow can be determined by the vortex system. This is indeed consistent with the far-field concept of the asymptotic analysis of the problem, which initiates the present formulation.

The model can therefore in principle be applied to cases with conditions and configurations different from those used for the present demonstration, provided that the inner conditions are specified. It is well-known that the vortex positions depend strongly on the nose shape and even on imperfections at the apex as a direct consequence of the fact that these factors directly govern the development of the three-dimensional boundary layer over the nose region. It is unlikely that a general correlation of the experimental data for the vortex positions will result. However, the upper bound of the forces can usually be established in the experiments,[9,14,15] and these conditions will be used to provide the inner conditions for the present model. It is interesting to note that the laminar and the turbulent separations generate very similar force variations.[14] The present inner conditions based on laminar separation may, after some modification, be applicable to the turbulent cases. The model is presently being examined further in the light of the foregoing evidence, with particular interest in applications to a body with conical noses.

Appendix: Asymptotic Analysis of Flow Past Long Slender Bodies at High Angles of Attack

Most of the flow prediction methods for a slender body at high angles of attack are based on the impulse flow

analogy,[16] with the analyses carried out at the crossflow plane. This assumes that the slender-body theory can be loosely applied, where in principle it is valid only at small angle of attack. No justification has yet been given for its application at high angles of attack.[1]

Conventional slender-body theory indeed cannot be applied to the present problem, which violates all the basic assumptions of the theory that the local inclination of the body surface to the freestream direction must be small.[17] However, the problem can be properly formulated in the same manner as the slender-body theory by an asymptotic analysis. For a long slender body at arbitrary angles of attack, two disparate length scales should be considered. In the far field, the characteristic length is the body length, and in the near field, it is the diameter of the body. If the body length is much larger than the diameter, as a long slender body implies, the problem admits a singular perturbation treatment.[18] The nature of the present problem is closely related to that of the lifting-line theory for swept wings, which also involves two disparate lengths.[19]

For simplicity of analysis, incompressible flow is considered. The flow is further assumed to be irrotational with concentrated vorticity; thus, a velocity potential can be introduced. A body-aligned Cartesian coordinate system (x',y',z') is used with the x' axis taken along the body in the downstream direction. The governing equation in terms of the velocity potential is thus the three-dimensional Laplace equation

$$\frac{\partial^2\Phi}{\partial x'^2}+\frac{\partial^2\Phi}{\partial y'^2}+\frac{\partial^2\Phi}{\partial z'^2}=0 \tag{A1}$$

The boundary conditions are the nonpermeable condition at the surface

$$\nabla\Phi\cdot\vec{n}=0 \tag{A2}$$

where $\vec{n}$ is the outward unit vector normal to the body surface. At infinity the disturbance vanishes.

For a slender body with the body length L much larger than the body diameter D, a perturbation procedure can be carried out with the ratio of these two scaling lengths as a perturbation parameter and with the near and far fields scaled by their appropriate lengths. For the inner region, the spatial variables are scaled as

$$\bar{x}'=\frac{x'}{L},\quad \bar{y}'=\frac{y'}{D},\quad \bar{z}'=\frac{z'}{D} \tag{A3}$$

and the perturbation potential

$$\phi=\Phi-Ux'\cos\alpha-Uz'\sin\alpha \tag{A4}$$

scaled by $DU\sin\alpha$, assuming $\sin\alpha\gg 0$. The latter can be expanded asymptotically for small $\epsilon=D/L$,

$$\bar{\phi}=\bar{\phi}_0+\epsilon\bar{\phi}_1+\epsilon^2\bar{\phi}_2\ldots \tag{A5}$$

where the normalized variables are marked with a bar. The perturbation equation for each order can now be written as

$$\frac{\partial^2\bar{\phi}_o}{\partial\bar{y}'^2}+\frac{\partial^2\bar{\phi}_o}{\partial\bar{z}'^2}=0 \tag{A6}$$

$$\frac{\partial^2\bar{\phi}_1}{\partial\bar{y}'^2}+\frac{\partial^2\bar{\phi}_1}{\partial\bar{z}'^2}=0 \tag{A7}$$

$$\frac{\partial^2\bar{\phi}_2}{\partial\bar{y}'^2}+\frac{\partial^2\bar{\phi}_2}{\partial\bar{z}'^2}=-\frac{\partial^2\bar{\phi}_o}{\partial\bar{x}'^2} \tag{A8}$$

The boundary condition at the body surface can be expanded in a similar manner. The resulting expressions for each order are

$$\frac{\partial\bar{\phi}_0}{\partial\bar{y}'}\frac{\partial f}{\partial\bar{y}'}+\left[1+\frac{\partial\bar{\phi}_o}{\partial\bar{z}'}\right]\frac{\partial f}{\partial\bar{z}'}=0 \tag{A9}$$

$$\frac{\partial\bar{\phi}_1}{\partial\bar{y}'}\frac{\partial f}{\partial\bar{y}'}+\frac{\partial\bar{\phi}_1}{\partial\bar{z}'}\frac{\partial f}{\partial\bar{z}'}+\frac{\partial f}{\partial\bar{x}'}=0 \tag{A10}$$

$$\frac{\partial\bar{\phi}_2}{\partial\bar{y}'}\frac{\partial f}{\partial\bar{y}'}+\frac{\partial\bar{\phi}_2}{\partial\bar{z}'}\frac{\partial f}{\partial\bar{z}'}+\frac{\partial\bar{\phi}_o}{\partial\bar{x}'}\frac{\partial f}{\partial\bar{x}'}=0 \tag{A11}$$

where $f(x',y',z')=0$ is the body shape.

The zero-order equation and the boundary condition constitute an exact two-dimensional flow problem. The first-order equation is still a two-dimensional one; the three-dimensional effect appears only as a local parameter in the boundary condition. The effect of the streamwise variation appears both in the equation and the boundary condition for the second-order correction. The crossflow approach used in the existing methods is therefore correct up to the first order.

The inner perturbation is invalid in the far field, and an outer perturbation has to be developed. The asymptotic solution for the outer flow near the body will then provide the outer boundary condition for the inner region. To analyze the outer region, the governing equation is cast in the wind coordinates (x,y,z) with the x axis along the freestream direction. In this region, the characteristic length scale is the body length L; thus, all spatial variables are scaled as

$$\bar{x}=\frac{x}{L},\quad \bar{y}=\frac{y}{L},\quad \bar{z}=\frac{z}{L} \tag{A12}$$

The perturbation potential can be similarly expanded for small ϵ:

$$\hat{\phi}=\frac{\phi}{Ud}=\hat{\phi}_o+\epsilon\hat{\phi}_1+\epsilon^2\hat{\phi}_2+\ldots \tag{A13}$$

All perturbation equations are now in the form of the three-dimensional Laplace equation

$$\frac{\partial^2\hat{\phi}_i}{\partial\bar{x}^2}+\frac{\partial^2\hat{\phi}_i}{\partial\bar{y}^2}+\frac{\partial^2\hat{\phi}_i}{\partial\bar{z}^2}=0,\quad i=0,1,2,\ldots \tag{A14}$$

The asymptotic solutions of the inner region provide the inner boundary conditions for the outer boundary value problem. It should be noted that the ϕ_o equation is of order ϵ because of the scaling of the spatial variables. The matching of the inner and outer solutions completes the formulation of the boundary value problem for the whole flowfield.

It should be noted that the present scaling also induces a nonuniformity in the nose region of the body in which the axial gradients become as important as the lateral ones. This region must be treated locally with the local solution matching the inner solution.[18]

The boundary value problem is now properly formulated. The near field is reduced to a two-dimensional crossflow problem up to the first order and has been treated in this manner in the existing methods.[1] The far field is a full three-dimensional problem, and the dynamics of the interacting vortex filaments is the dominant feature of the flow. The application of the far-field solution with information from the inner region forms the basic approach for the wake structure modeling presented in this paper.

For compressible flow, the analysis can be carried out in a similar manner, except that the conservation equations have to

be used with the shock jump conditions for transonic and supersonic flows. It can be shown that the zero-order inner problem is reduced to a two-dimensional form and the crossflow solution is valid at the limit of an infinitely long body. Because of the density variation, the first-order equation contains zero-order solutions in the coefficients additional to that in the boundary condition. The outer region is fully three dimensional. Again, matching of the inner and outer solutions is required for completion of the formulation.

The impulse flow analogy[16] often used in the treatment of the inner problem can also be clarified within the context of the present analysis. The analogy is basically the treatment of the development of the flow in the crossflow plane to that of the flow about an impulsively started cylinder, with the body axis corresponding to the time axis of the impulsive flow. A similar expansion transforming a three-dimensional steady-flow problem to a two-dimensional unsteady flow with the time variables corresponding to the length variable along the body can be found in the hypersonic small-disturbance theory.[20] This results from the fact that the perturbation velocity component u along the body is one order higher than the lateral components v and w (while for the present analysis, the velocity components are considered to be of the same order). For the present problem of a long slender body at high incidence, this condition would be satisfied if the trailing vortices inclined only slightly to the body axis. This is indeed the case for flows over the body at low and moderate angles of attack. However, one must be cautious in applying the results of this analysis (for inviscid flows) to a real viscous flow; e.g., the three-dimensional separation along the body may not be similarly analogized to the unsteady two-dimensional separation in the crossflow plane.

References

[1]Wardlaw, A.B. Jr., "High-Angle-of-Attack Missile Aerodynamics," Lecture 5, Missile Aerodynamics, AGARD-LS-98, Feb. 1979.

[2]Hunt, B.L., "Asymmetric Vortex Forces and Wakes on Slender Bodies," AIAA Paper 82-1336, Aug. 1982.

[3]Ericsson, L.E. and Reding, J.P., "Review of Vortex-Induced Asymmetric Loads, Part I," *Z. Flugwiss. Weltraumforsch,* Vol. 5, No. 3, 1981, pp. 162–174.

[4]Ericsson, L.E. and Reding, J.P., "Review of Vortex-Induced Asymmetric Loads, Part II," *Z. Flugwiss. Weltraumforsch.,* Vol. 5, No. 3, 1981, pp. 349–366.

[5]Lamont, P.J. and Hunt, B.L., "Prediction of Aerodynamic Out-of-Plane Forces on Ogive-Nosed Circular Cylinders," *Journal of Spacecraft,* Vol. 14, No. 1, Jan. 1977, pp. 38–44.

[6]Coe, P.L. Jr., Chambers, J.R., and Letko, W., "Asymmetric Lateral-Directional Characteristics of Pointed Bodies of Revolution at High Angles of Attack," NASA TN D-7095, Nov. 1972.

[7]Jorgensen, L.H., "Prediction of Aerodynamic Characteristics for Slender Bodies Alone and with Lifting Surfaces to High Angles of Attack," *High Angle of Attack Aerodynamics,* Paper 28, AGARD CP-247, 1978.

[8]Glauert, H., *The Elements of Aerofoil and Airscrew Theory,* 2nd Edition, Cambridge University Press, 1948, Chap. 10.

[9]Lamont, P.J. and Hunt, B.L., "Pressure and Force Distribution on a Sharp-nosed Circular Cylinder at Large Angles of Inclination to a Uniform Subsonic Stream," *Journal of Fluid Mechanics,* Vol. 76, Part 3, 1976, pp. 519–559.

[10]Clark, W.H., "Body Vortex Formation on Missiles in Incompressible Flows," AIAA Paper 77-1154, Aug. 1977.

[11]Champigney, P., "Reynolds Number Effect on the Aerodynamic Characteristics of an Ogive-Cylinder at High Angles of Attack," AIAA Paper 84-2176, 1984.

[12]Thomson, K.D. and Morrison, D.F., "The Spacing, Position and Strength of Vortices in the Wake of Slender Cylindrical Bodies at Large Incidences," *Journal of Fluid Mechanics,* Vol. 50, Part 4, 1971, pp. 751–783.

[13]Smith, Ll.H. and Nunn, R.H., "Aerodynamic Characteristics of an Axisymmetric Body Undergoing a Uniform Pitching Motion," Rept. NPS-59NN75021, Naval Graduate School, Monterey, CA, Feb. 1975.

[14]Lamont, P.J., "Pressure Measurements on an Ogive-Cylinder at High Angles of Attack with Laminar, Transitional, or Turbulent Separation," AIAA Paper 80-1556, 1980.

[15]Lamont, P.J., "The Complex Asymmetric Flow Over a 3.5D Ogive Nose and Cylindrical System Body at High Angles of Attack," AIAA Paper 82-0053, 1982.

[16]Allen, H.J. and Perkins, E.W., "A Study of the Effect of Viscosity on Flow Over Slender Inclined Bodies of Revolution," NACA Rept. 1048, 1951.

[17]Ashley, H. and Landahl, M., *Aerodynamics of Wings and Bodies,* Chapter 6, Addison-Wesley, MA, 1965.

[18]Van Dyke, M., *Perturbation Methods in Fluid Mechanics,* Chapter 4, Academic Press, New York, 1984.

[19]Cheng, H.K., Chow, R., and Melnik, R.E., "Lifting-Line Theory of Swept Wings Based on the Full Potential Theory," *Journal of Applied Mathematics and Physics* (ZAMP), Vol. 32, 1981, pp. 481–495.

[20]Hayes, W.D. and Probstein, R.F., *Hypersonic Flow Theory,* 2nd Ed., Vol. 1, Inviscid Flows, Chapter 2, Academic Press, New York, 1966.